Journal of the European Ceramic Society **13** (1994) 529–544

Development, Characterization and Oxidation Behaviour of Si_3N_4–Al_2O_3 Ceramics

J. Vleugels & O. Van Der Biest*

Department of Metallurgy and Materials Engineering (MTM), Katholieke Universiteit Leuven, De Croylaan 2, B-3001 Leuven, Belgium

(Received 11 August 1993; revised version received 20 December 1993; accepted 6 January 1994)

Abstract

Five Si_3N_4–Al_2O_3 ceramic grades were prepared by hot pressing at 1650°C. Backscattered electron micrographs revealed four different phases. Quantitative electron probe microanalysis allowed the identification of these phases as X-sialon, α-Al_2O_3, O'-sialon and β-sialon. The maximum solubility of Al_2O_3 in Si_3N_4 and in Si_2N_2O at 1650°C was determined as well as the chemical composition of X-sialon. Based on these results, a slightly revised phase diagram is proposed. The general features describing the microstructure of the various phases have been investigated by transmission electron microscopy. The influence of the various phases on the mechanical properties was investigated; hardness, fracture toughness and elastic modulus were measured. The oxidation behaviour has been studied in air at 1300°C and 1450°C. The metastable phase diagram of Al_2O_3–SiO_2 in the absence of mullite can be used to predict the oxidation products and relative amounts formed in the oxide layers.

Fünf keramische Si_3N_4–Al_2O_3 Werkstoffe wurden mittels Heißpressen bei 1650°C hergestellt. Rasterelektronenmikroskopische Beobachtungen zeigten verschiedene Phasen die mittels Mikrosonden-Analyse als X-sialon, α-Al_2O_3, O'-sialon und β-sialon identifiziert werden konnten. Die Maximallöslichkeit von Al_2O_3 in Si_3N_4 und Si_2N_2O bei 1650°C, und die chemische Zusammensetzung des X-sialon wurden ermittelt. Aufgrund der experimentellen Daten konnte das Phasendiagramm bei 1650°C modifiziert werden. Das Mikrogefüge der sialonen wurde mit Transmissionselektronenmikroskopie charakterisiert und der Einfluß der verschiedenen Phasen auf die mechanischen Eigenschaften der Keramik; Härte, Bruchwiderstand und Elastizitätsmodul wurden bestimmt. Die Oxidationsempfindlichkeit des Si–Al–O–N Werkstoffes wurde geprüft in Luft bei 1300°C und 1450°C. Das Phasendiagramm des Al_2O_3–SiO_2-Systems in Abwesenheit von Mullit konnte dazu benutzt werden, die Oxidationsprodukte und ihre Relativverhältnisse vorherzusagen.

Cinq céramiques à base de Si_3N_4–Al_2O_3 ont été préparées par frittage sous charge. Des images à base d'électrons rétrodiffusés permettaient de distinguer des phases différentes qui ont été identifiées comme X-sialon, α-Al_2O_3, O'-sialon et β-sialon par microsonde électronique. La composition chimique de la phase X-sialon ainsi que la solubilité maximale de Al_2O_3 dans Si_3N_4 et dans Si_2N_2O à 1650°C ont été déterminées. Selon les résultats obtenus, le diagramme de phase a été légèrement révisé. La microstructure des céramiques a été étudiée à l'aide de la microscopie électronique à transmission. Les propriétés mécaniques des sialons; la dureté, la ténacité et le module d'élasticité ont été evaluées. La résistance à l'oxidation a été étudiée dans l'air à 1300°C et 1450°C. Le diagramme de phase du système Al_2O_3–SiO_2 en absence de la mullite permettrait de prévoir les produits d'oxidation et leurs quantités relatifs.

1 Introduction

The excellent thermal and mechanical properties of Si_3N_4 have resulted in extensive research on this material during the last 20 years. As a consequence of the predominantly covalent bonds, the self-diffusion coefficients in Si_3N_4 are too low to obtain dense materials by classical sintering methods.[1] Full density, however, can be obtained by liquid-phase sintering. Most commonly used sintering additives are Y_2O_3, MgO, AlN, SiO_2, Al_2O_3 and rare earth oxides.[1,2] The addition of sintering aids results in the formation of an

* To whom correspondence should be addressed.

amorphous grain boundary phase, limiting the mechanical properties of Si_3N_4-based materials at high temperatures. Al_2O_3, however, can, to a certain extent, be dissolved into Si_3N_4.[3,4] Si^{4+} and N^{3-} are then substituted by Al^{3+} and O^{2-}, leading to the formation of an expanded β-Si_3N_4 lattice, designated as β-sialon or β', with a general formula of $Si_{6-z}Al_zO_zN_{8-z}$ ($z \leq 4{\cdot}2$ at 1750°C). Dense single-phase β-sialon ceramics have been studied by several authors.[5–7] According to the quasi-ternary Si_3N_4–Al_2O_3–AlN–SiO_2 phase diagrams[3,8] addition of Al_2O_3 to Si_3N_4 will result in the formation of multi-phase sialon ceramics, containing O'-sialon, X-sialon, Al_2O_3 and β-sialon. Although Si_2N_2O was already discovered in 1926,[9] information is scarce about the mechanical, thermal and thermodynamic properties of Si_2N_2O and the O'-phase, being a solid solution of Si_2N_2O and Al_2O_3. X-Sialon is still the subject of much controversy in literature. The exact chemical composition is controversial. More than nine different chemical compositions could be found ranging from 43 to 60 eq.% aluminium and 42 to 84 eq.% oxygen.[3,4,8,10–16] Little is known about the properties of pure X-sialon material.

The high oxidation resistance of Si_3N_4 and related sialon materials is dependent on the formation of a protective surface oxide layer. Sintering additives in these materials, such as Y_2O_3 and MgO, cause the formation of secondary phases which greatly influence the oxidation behaviour.[17–20]

Infrared reflection spectroscopy and X-ray diffraction studies on the oxidation of single-phase β-sialons showed that the oxide layer consisted of cristobalite, mullite and a glass phase.[21,22] The amount of cristobalite and glass phase decreases while the amount of mullite increases with increasing substitution level. Differences in weight gain for a range of single-phase β-sialons could only be found at temperatures of 1300°C and higher.[20] At these temperatures, weight gain decreased with increasing aluminium and oxygen content.

This paper reports on the development and characterization of five different Si_3N_4–Al_2O_3 ceramic grades without addition of other sintering aids. The chemical compositions of the different phases, the microstructure and the mechanical properties of the prepared materials are investigated. The relative oxidation behaviour of these ceramics is determined by acquiring weight gain versus time plots. Possible oxidation mechanisms are explained, and oxidation products are characterized by electron probe microanalysis (EPMA) and X-ray diffraction (XRD) investigation of the surface and cross-sections of the oxide layer formed on the oxidized specimens.

2 Experimental

Commercial Si_3N_4 powder, HCST grade LC 12-SX (97% α, submicron particle size, 1·8–2·1 wt% oxygen) and Al_2O_3 powder, Baikowski, grade SM8 (95% α, submicron particle size), were used to prepare powder mixtures with a composition along the Si_3N_4–Al_2O_3 line in the phase diagram, shown in Fig. 1. The chemical composition of the powder mixtures is given in Table 1. The five powder mixtures were chosen so that there is at least one composition in each two- or three-phase region, according to the phase diagram determined by Naik *et al.*[8] The oxygen content of the Si_3N_4 powder was not taken into account so that in reality the starting compositions are a little above the Si_3N_4–Al_2O_3 line.

100 g powder was mixed in a multidirectional mixer (type turbula) for 72 h in a polyethylene bottle containing 350 g alumina milling balls and 1 litre *n*-propanol. The weight loss of the alumina balls could be neglected. After evaporation of the propanol, 14 g of the powder mixture was inserted into a graphite container, coated with boron nitride. After cold precompression at 40 MPa, the samples were hot pressed in an electrical resistance heating furnace (under vacuum of 0·1 Pa because of the graphite heating element), for 1 h at 1650°C with a mechanical load of 30 MPa. The samples are separated from the furnace atmosphere by the graphite hot press set-up, while the sliding contacts are sealed by the boron nitride. Although

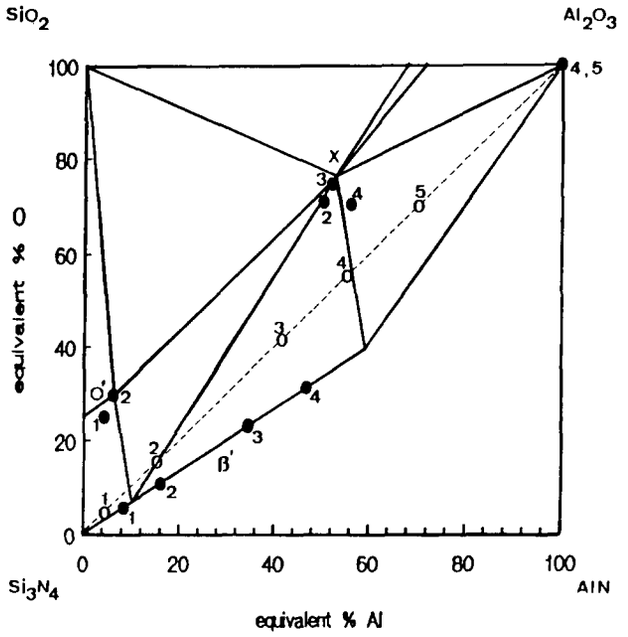

Fig. 1. Chemical composition of starting powder mixtures and formed phases, given in the subsolidus phase diagram.[8] The numbers on the phase diagram refer to the five different Si_3N_4–Al_2O_3 ceramics and either indicate the starting composition (○) of a grade or the chemical composition of one of the phases (●) found in the respective sialon grade.

Table 1. Compositions (wt%) of starting powder mixtures

	Sialon				
	1	*2*	*3*	*4*	*5*
Si_3N_4	93·72	79·55	49·68	35·96	22·73
Al_2O_3	6·28	20·45	50·12	64·04	77·27

no special care was taken on the nitrogen pressure in the hot press, the weight loss of the samples was less than 1%. The hot-pressed samples had a diameter of 30 mm and a height of 5 mm.

After removal of the boron nitride, XRD patterns of ground surfaces of the samples were acquired with a Philips diffractometer equipped with a Cu K_α source. Qualitative identification of the patterns was done using the JCPDS[23] data files. KCl, dusted on the surface of the specimens, was used as an internal marker for unit cell parameter measurements.

The density of the hot-pressed specimens was determined by the water displacement method.

Specimens for SEM were smoothly polished and coated with a thin carbon layer. Back-scattered electron images were taken on a Jeol 733 microprobe.

For TEM investigation, thin slices of material were cut to a thickness of 300 micron. Small 3 mm discs were cut ultrasonically from these polished slices and the centre was dimpled down to a thickness of less than 50 micron. Final preparation was done by argon ion bombardment, in a Gatan 600 ion-milling instrument, until the samples were penetrated. TEM characterization was done on a Jeol C 200 microscope.

Quantitative chemical analysis was done by EPMA (Jeol 733), using a pure SiO_2 and Al_2O_3 standard. Samples and standards were coated simultaneously with a very thin gold layer, to ensure a homogeneous coating thickness. Quantitative analysis was performed for Si, Al and O. N was calculated by difference. The reported values are the mean of at least ten measurements.

Vickers hardness, H_{V_5}, was measured on a Zwick hardness tester. Fracture toughness, K_{IC}, values were obtained by the Vickers indentation technique, based on crack length measurements of the radial crack pattern produced by Vickers H_{V_5} indentations. K_{IC} values were calculated using the formula of Anstis *et al.*[24] The elastic modulus, E, of the specimens was measured by the resonance frequency method on a Grindo-sonic apparatus.

Oxidation experiments were done in a Kanthal furnace in air for 160 h at 1300°C and for 100 h at 1450°C. At preset time intervals, the samples were cooled to room temperature to determine their weight gain. Small rectangular bars (2 × 6 × 28 mm) were machined out of the hot-pressed samples. After ultrasonic cleaning and weight determination, the five sialon bars were put together in an alumina crucible. To prevent contamination from the refractory material in the furnace, alumina plates were used to cover most of the crucible.

3 Results and Discussion

3.1 Microstructural characterization of Si_3N_4–Al_2O_3 ceramics

3.1.1 Density

The densities of the materials are given in Table 2. The density of single-phase β-sialon can be calculated[5] as (3·20–0·041 z) g cm^{-3}. X-Sialon[11] has a density of ≈3·01 g cm^{-3} and the density of O'-sialon will decrease slightly from that of silicon oxynitride (2·82 g cm^{-3}). The theoretical density calculations, based on the estimated weight proportions of the phases in each ceramic (see Table 3), indicate that all sialon ceramics reached at least 96% of the theoretical density. These values, however, should be seen as approximate values, because of the difficulties in determining the accurate volume fractions of the different phases in these sialon ceramics. Indeed, optical microscope and SEM investigation showed no porosity in sialons 1 and 5. The central part of the hot-pressed discs of sialons 2, 3 and 4, however, showed a low amount of remaining closed porosity, while the edges reached full density.

Table 2. Densities (g cm^{-3}) of the different sialon ceramics

	Sialon				
	1	*2*	*3*	*4*	*5*
Measured density	2·98	2·97	2·99	3·09	3·26
Theoretical density	3·09	3·09	3·07	3·10	3·38
% TD	96·6	96·2	97·6	99·7	96·4

Table 3. Chemical composition of the hot pressed Si_3N_4–Al_2O_3 ceramics

Sialon	*β-sialon*[a]		*O'-sialon*		*X-sialon*	Al_2O_3
	z	(wt%)	x	(wt%)	(wt%)	(wt%)
1	0·65	77	0·12	23	0	0
2	1·22	79	0·16	17	4	0
3	2·47	62	—	0	38	0
4	3·23	43	—	0	50	7
5	2·97	26	—	0	34	40

[a] The substitution levels of sialons 1–4 were obtained from EPMA analysis, whereas that of sialon 5 was obtained from XRD measurements.

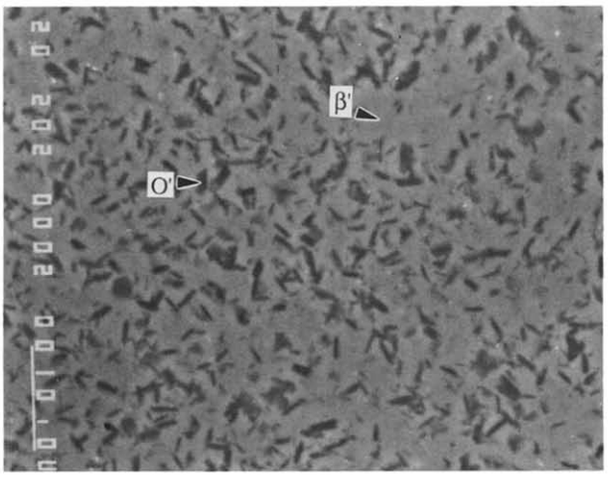

(a)

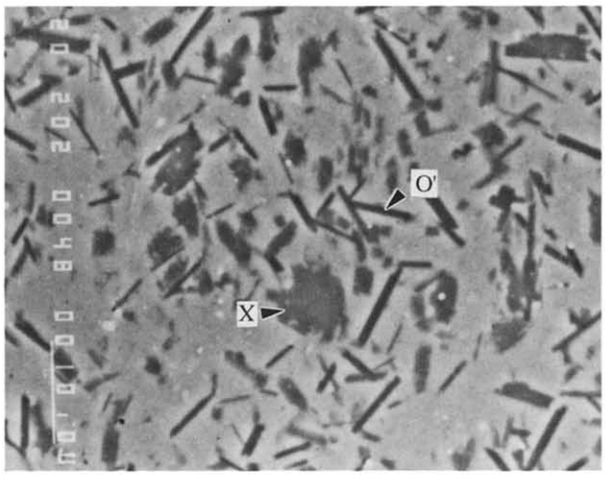

(b)

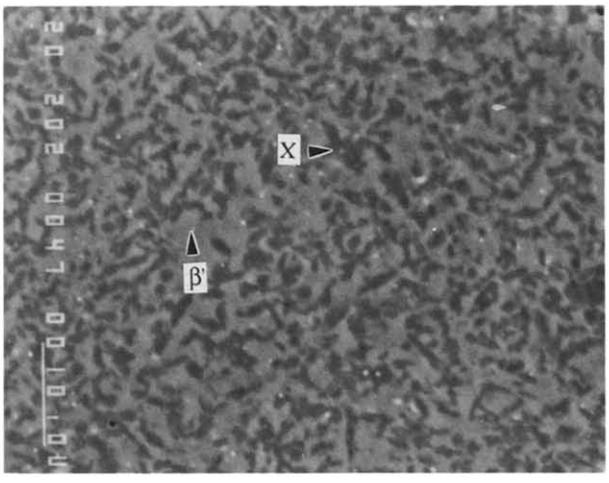

(c)

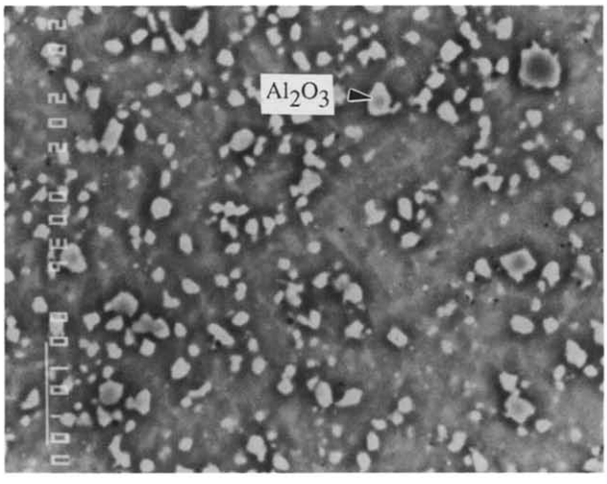

(d)

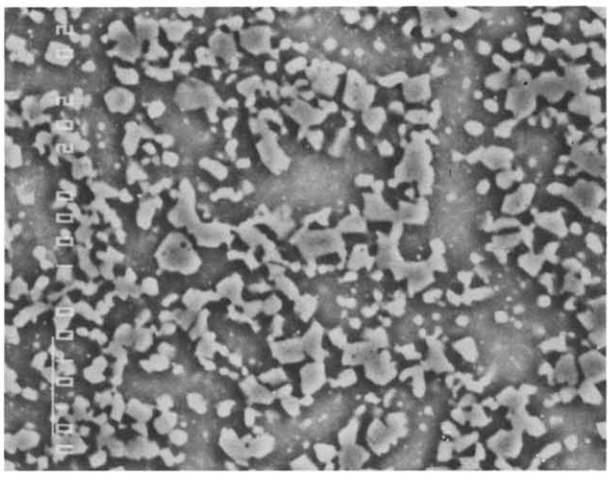

(e)

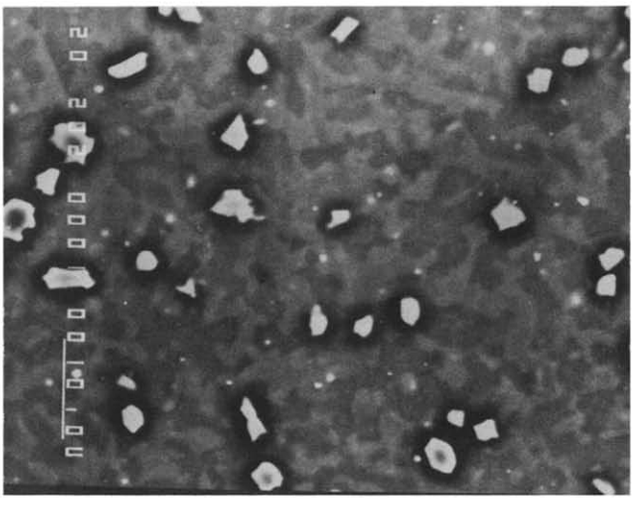

(f)

Fig. 2. Backscattered electron micrographs of the different Si–Al–O–N ceramics hot pressed at 1650°C. (a) Sialon 1, (b) sialon 2, (c) Sialon 3, (d) sialon 4 and (e) sialon 5. (f) Microstructure of sialon 4, hot pressed at 1750°C.

Table 4. Unit cell parameters (nm) and substitution level of the β-sialon phase

	Sialon				
	1	*2*	*3*	*4*	*5*
a Axis	0·763 6	0·764 9	0·768 7	0·770 6	0·769 9
c Axis	0·292 4	0·293 3	0·296 7	0·297 5	0·297 6
z Value	0·90	1·28	2·59	3·06	2·97

3.1.2 X-Ray phase analysis

Since no α-Si_3N_4 diffraction signals could be detected in the hot-pressed samples, the α to β Si_3N_4 conversion is completed in all sialons.

Good agreement between the identified phases, summarized in Table 3, and those that might be expected according to the subsolidus phase diagram[8] is found for all sialons, except the appearance of alumina in sialon 4. The appearance of alumina in sialon 4 implies that the maximum substitution level of the β-sialon at 1650°C is less than might be expected from the phase diagram at 1650°C,[25] and the subsolidus diagram at 1450°C (Fig. 1).

The unit cell parameters of the β'-phase, listed in Table 4, increase from sialon 1 to 4, indicating the expansion of the β-Si_3N_4 lattice by the substitution of Si^{4+} and N^{3-} by Al^{3+} and O^{2-}. Sialons 4 and 5 have the same unit cell parameters, with a maximum substitution level of $z \approx 3$. The substitution level was calculated from the unit cell parameters according to the equations reported by Ekström *et al.*[5] The unit cell parameters of the orthorhombic O'-sialon phase increase with increasing substitution level, as a result of the replacement of Si–N (0·174 nm) bonds by Al–O (0·175 nm) bonds. The unit cell parameters of alumina found in sialons 4 and 5 are the same as the literature values found for pure α-alumina.

3.1.3 Scanning electron microscopy

The backscattered electron micrographs of sialon 1 (Fig. 2(a)) and 2 (Fig. 2(b)) show small dark elongated O'-grains embedded in a bright β-sialon matrix. The aspect ratio of the O'-sialon grains in sialon 2 is larger than in sialon 1. The morphology of the β-sialon particles is not clear from these pictures. Besides O'- and β-sialon, dark, irregularly shaped grains can be distinguished in sialon 2. These grains were identified as X-sialon. Sialon 3 (Fig. 2(c)) consists of bright β-sialon and dark X-sialon.

In sialon 4 (Fig. 2(d)), isolated bright α-Al_2O_3 grains can be seen. In between these grains, the darker X-sialon can still be distinguished from the brighter β'-phase. The reason for the brightness of the alumina particles is the interference of topographical contrast in this picture. Because of the higher hardness of alumina, β-sialon and X-sialon are preferentially polished away, causing a small etching effect.

Sialon 5 (Fig. 2(e)) is dominated by large isolated α-alumina grains. In between these grains there is β-sialon; the presence of X-sialon material is not clear from these micrographs.

3.1.4 Transmission electron microscopy

The O'-sialon grains in sialons 1 and 2 can easily be distinguished from the hexagonal β-sialon grains, not only by their elongated morphology but also by their characteristic striations (Fig. 3(a)), caused by a high stacking fault density parallel to the (100) planes of the orthorhombic structure.[26]

The X-sialon grains in sialons 3 to 5 show a characteristic twin pattern (Fig. 3(b)). The crystal structure of X-sialon is triclinic, as determined by

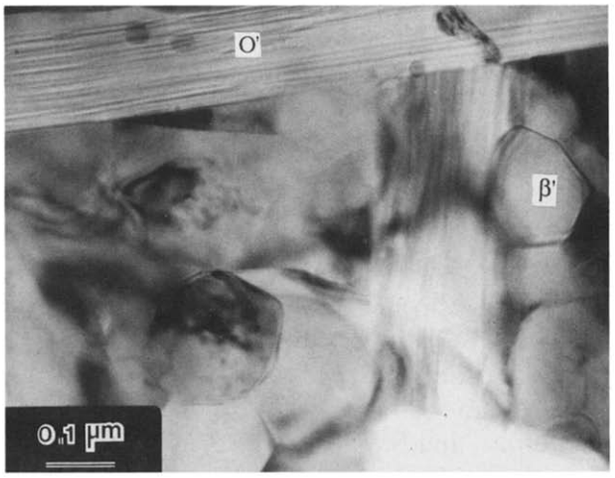

(a)

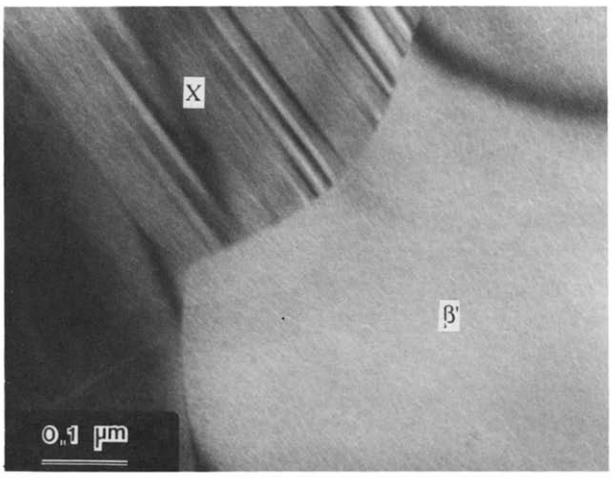

(b)

Fig. 3. TEM micrographs of argon ion thinned sialon samples. (a) The presence is shown of elongated O'-sialon grains in sialon 1, containing a high stacking fault density. (b) X-sialon grains, with a characteristic twin pattern, are shown in sialon 3.

electron diffraction analysis and has lattice parameters similar to those reported by Zangvil.[10]

Within the resolution limits of the microscope, no intergranular amorphous phase could be observed at the grain boundaries or the triple junctions in the five different sialon materials. The existence of a very small grain-boundary phase, however, a few atomic layers thick and formed by impurities in the starting powders, is not excluded.

3.2 EPMA analysis of the different phases

The compositions of the starting powder mixtures and the chemical compositions of the different phases analysed in the hot-pressed samples are plotted on the phase diagram in Fig. 1. The substitution levels z and x for β-sialon ($Si_{6-z}Al_zO_zN_{8-z}$) and O'-sialon ($Si_{2-x}Al_xO_{1+x}N_{2-x}$) are listed in Table 3.

A maximum solubility of Al_2O_3 in Si_2N_2O was reached in sialon 2. The substitution level, x, of the O'-sialon grains in sialon 2, calculated from EPMA analysis, varies from 0·16 to 0·19 for the different sialon 2 samples analysed. These values are in good agreement with the values reported by Trigg & Jack.[27] A maximum substitution level of 0·20 at 1800°C was reported. The point of maximum solubility is in perfect agreement with the subsolidus phase diagram.[8]

The chemical composition of X-sialon in sialons 2 and 3, $Si_{16·8}Al_{22·4}O_{47·8}N_{13·0}$ and $Si_{16·4}Al_{23·6}O_{48·8}N_{11·2}$, respectively, is very close to the literature value, $Si_{15·6}Al_{23·4}O_{50·6}N_{10·4}$ or $Si_{12}Al_{18}O_{39}N_8$, reported by Naik *et al.*[8] Based on the results obtained from different starting compositions, $Si_{12}Al_{18}O_{39}N_8$ was suggested to be a closer formula, rather than $Si_3Al_6O_{12}N_2$ and $Si_2Al_3O_7N$, by Anya & Hendry.[28] The composition found in sialon 4 is somewhat different. This might be caused by the size of the interaction volume of the electron beam. It may be concluded that X-sialon is situated on the Si_3N_4–$3Al_2O_3 \cdot 2SiO_2$ (mullite) line in the phase diagram.

The substitution levels for β-sialon (see Table 3) correspond well with those obtained from XRD analysis (see Table 4). Analysis results for the β'-phase of sialon 5 were not obtained because of the impossibility of excluding alumina grains from the analysed volume. From XRD measurements, the substitution level of the β-sialon phase of sialons 4 and 5 is the same. The presence of Al_2O_3 in sialons 4 and 5 suggests a maximum substitution level in the β'-phase of these ceramics. The substitution level of $z = 3$ is less than might be expected from the existing phase diagrams at 1650°C[25] or the subsolidus diagram at 1450°C (see Fig.1). Nor can it be deduced from the recently revised phase diagram at temperatures of 1700–1775°C.[16] The limited extension of the β'-phase suggests a slightly revised phase diagram at 1650°C, as shown in Fig. 4.

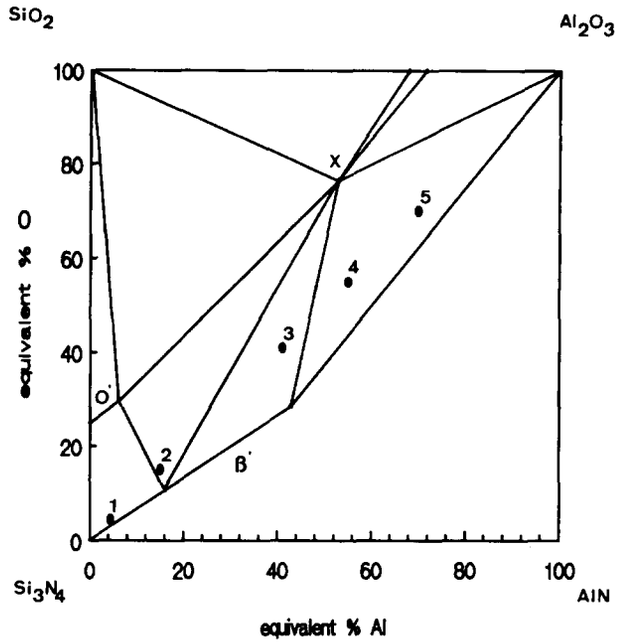

Fig. 4. Revised Si_3N_4–SiO_2–Al_2O_3–AlN phase diagram at 1650°C, including the starting powder mixture compositions of the investigated ceramics.

The present findings on sialons 2, 3, 4 and 5 are also in disagreement with a recent thermodynamic assessment of the Si–Al–O–N system by Hillert & Jonsson.[29] Figure 5 shows the calculated section at 1650°C, in comparison with the present experimental data. The substitution level of β-sialon in sialons 4 and 5 is less than might be expected from the calculated diagram, sialon 2 is a β–O'–X-

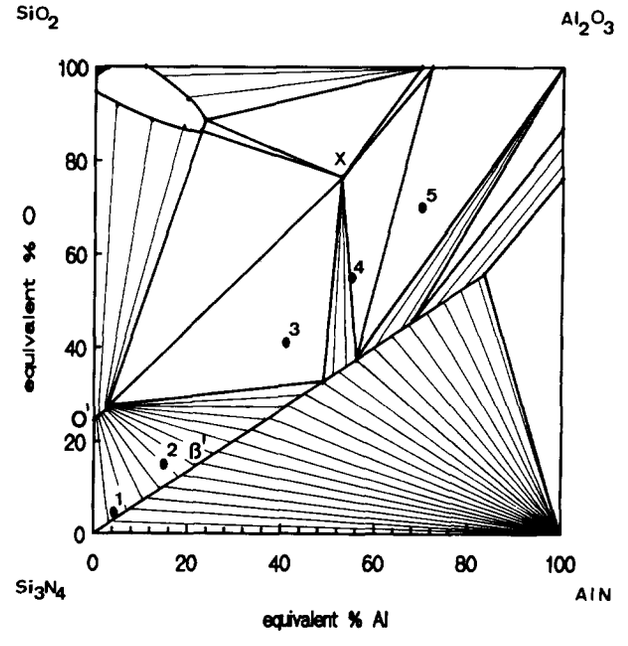

Fig. 5. Calculated section of the Si_3N_4–SiO_2–Al_2O_3–AlN phase diagram at 1650°C according to Hillert and Jonsson,[29] in comparison with the experimental data of this study. (1) β–O', (2) β–O'–X, (3) β–X, (4) X–β–Al_2O_3 and (5) Al_2O_3–β–X.

sialon whereas sialon 3 was found to be a β–X mixture. No evidence of mullite was found in sialon 5, making the existence of the mullite–β-sialon two-phase region at 1650°C doubtful.

To investigate the influence of the hot-press temperature on the substitution level of the β-sialon phase, the powder mixture of sialon 4 was hot pressed at 1750°C. The microstructure of the obtained ceramic is shown in Fig. 2(f). Compared to the ceramic hot pressed at 1650°C (see Fig. 2(d)), the amount of Al_2O_3 is decreased, while the amount of X-sialon and β-sialon increased. EPMA results showed that the substitution level of the β'-phase increased from 3·23 in the ceramic hot pressed at 1650°C to 3·47 in the sample hot pressed at 1750°C. These results clearly show that the substitution level of the β-sialon phase is influenced by the densification temperature. The measured substitution level of 3·47 is below the maximum substitution level of 4·2 at 1760°C, as reported by Gauckler *et al.*[13] The maximum extension of the β-sialon solid solution is not very clear from literature values. At 1823°C, the upper composition limit of the β-sialon phase in hot isostatic-pressed ceramics[5] was found to be 3·85 at 200 MPa pressure and about 4·1 at atmospheric pressure, whereas a limiting value of about 4·2 at 1700°C and 2·0 at 1400°C are reported by Jack.[30] According to the phase diagram[31] at 1750°C, the substitution level for the β-sialon phase in sialon 4 will be ≈3·7, which is more in agreement with the present result at 1750°C.

A good estimate of the weight proportions of the phases in each sialon grade could be obtained by application of the lever rule in the quadrilateral representation of the Si_3N_4–AlN–Al_2O_3–SiO_2 system.[32] The weight proportions for sialon 5 were calculated based on the substitution level for the β'-phase obtained from XRD measurements (see Table 4) because of the impossibility of excluding the small Al_2O_3 grains from the analysed volume and the problems in differentiating the β-sialon from X-sialon by EPMA (see Fig. 2(e)).

3.3 Mechanical properties

The hardness (H_{V_5}), fracture toughness (K_{IC}) and elastic modulus (E) of the hot-pressed sialons were measured and are given in Table 5.

The hardness and fracture toughness of sialons 1 and 2 are in good agreement with those values reported for single-phase β-sialon materials.[5] Fracture toughness values of single-phase β-sialon materials are reported to decrease from 3 to 2·5 with increasing substitution level (a constant E modulus of 300 GPa was used in these calculations). The decrease of hardness and fracture toughness with increasing substitution level can be explained by the grain growth stimulating effect of the added Al_2O_3. The K_{IC} value for sialon 1 is a little higher than the highest K_{IC} value reported for single-phase β-sialons.

Table 5. Hardness (H_{V_5}), fracture toughness (K_{IC}) and elastic modulus (E)

Sialon	H_{V_5} *(kg/mm²)*	E *(GPa)*	K_{IC} *(MPa m$^{1/2}$)*
1	1 657	266	3·4
2	1 629	163	2·0
3	1 460	190	1·4
4	1 464	221	1·6
5	1 554	285	2·3

The hardness and fracture toughness of sialons 3 and 4 are below the reported single-phase β-sialon values. This can only be related to the high amount of X-sialon present in both materials. No hardness, fracture toughness or E values for pure X-sialon could be found in literature.

The fracture toughness increase from sialon 3 to 5 is related to the crack deflecting effect of isolated alumina grains, as illustrated in Fig. 6. Because of the intrinsic properties of alumina, the hardness and elastic modulus increases with increasing amount of alumina in sialons 4 and 5.

3.4 Oxidation behaviour of Si_3N_4–Al_2O_3 ceramics

3.4.1 Oxidation products formed at 1300°C and 1450°C

The different oxidation products determined by XRD and EPMA after 160 h at 1300°C and 100 h at 1450°C are listed in Table 6.

The amorphous aluminosilicate phase in the oxide layers formed at 1300°C and 1450°C contains a low amount of Ca^{2+}, Mg^{2+} and Na^{+}. These elements are thought to be diffusing outwards from the grain boundaries in the sialon material into the oxide layer during oxidation, because of

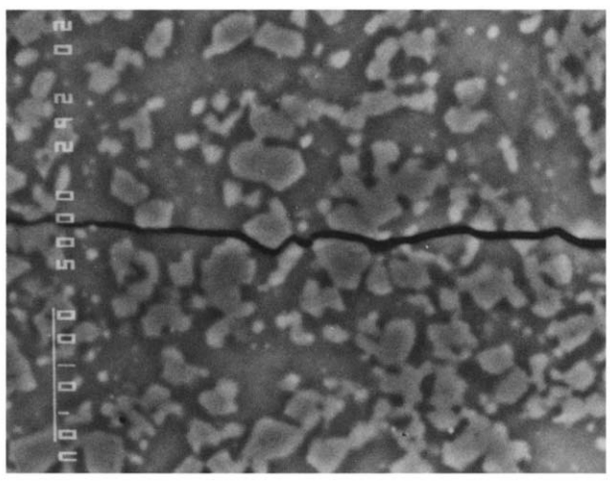

Fig. 6. Crack deflection by alumina grains in sialon 5.

Table 6. Oxidation products at 1300°C and 1450°C

	Sialon				
	1	*2*	*3*	*4*	*5*
Cristobalite	*				
Mullite		*	*	*	*
Aluminosilicate glass	*	*	*	*	

the difference in chemical potential of these ions at the grain boundaries and in the aluminosilicate.[17,19] The same was observed for Al^{3+} ions.[20] Ca^{2+}, Mg^{2+}, Na^+ and K^+ ions tend to lower the viscosity of the aluminosilicate glass, and hence enhance O_2 transport through the oxide layer.[18] This viscosity reducing tendency of impurity ions is counteracted by the presence of Al^{3+}.[17,18] The amount of Al in the aluminosilicate glass increased with increasing Al_2O_3 content in the starting powder.

Very good agreement was found between the oxidation products determined in the oxide layers and those that might be predicted from the metastable phase diagram of Al_2O_3–SiO_2 in the absence of mullite,[33] shown in Fig. 7. This diagram turned out to be a useful tool in predicting the relative amounts and types of oxidation products formed in the oxide layers of Si_3N_4–Al_2O_3 materials in air at 1300°C and 1450°C. Two adjustments have to be made. First of all the formation of mullite is favoured. This is not surprising, since mullite formation is typically observed at 980°C, if the scale of chemical homogeneity is at the atomic

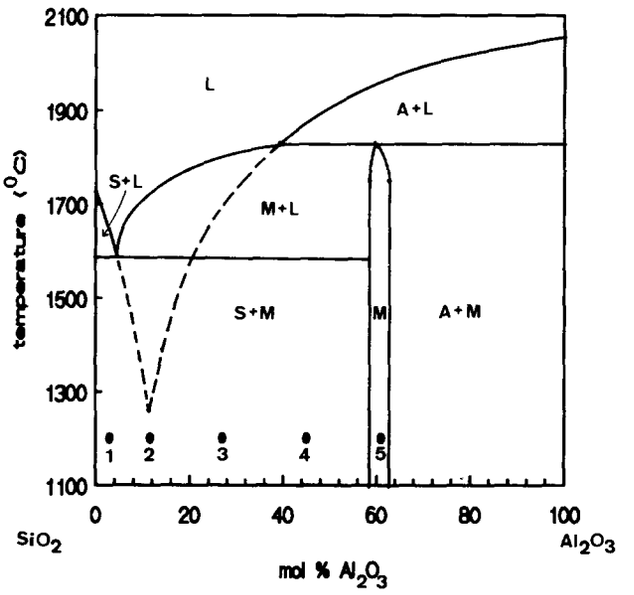

Fig. 7. SiO_2–Al_2O_3 equilibrium phase diagram.[33] Superimposed on the stable equilibrium diagram, shown by the solid lines, is the metastable phase diagram, formed by the extensions of the SiO_2 and Al_2O_3 liquidi in the absence of mullite. The molar compositions at the oxidation front of the five different sialon materials are plotted and marked with their respective numbers on the diagram. L, Liquid, A, alumina, S, silica and M, mullite.

level.[34] Secondly, the liquid phase formed during oxidation does not crystallize during fast cooling. The molar compositions of Al_2O_3 and SiO_2 at the oxidation front of the five different sialons, calculated from the initial composition of the starting powders, are plotted on the phase diagram (Fig. 7). The oxide layers of sialons with an overall molar composition at the oxidation front below the eutectic composition (≈88 mol% SiO_2 and ≈12 mol% Al_2O_3) will consist of cristobalite and an amorphous aluminosilicate phase. At compositions above the eutectic, mullite and aluminosilicate are formed.

3.4.2 Oxidation at 1300°C

The surface of the oxidized specimens and cross-sections perpendicular to the oxide layer were investigated by EPMA. Scanning electron micrographs of the surfaces formed in air after 160 h at 1300°C, for the five different sialon materials, are shown in Fig. 8. The corresponding cross-sections are given in Fig. 9.

The cross-sectioned oxide layer of sialon 1 (Fig. 9(a)) shows the formation of N_2 gas bubbles (black circles) at the oxidation front, penetrating through a chain of larger SiO_2 crystals (dark) and the outer aluminosilicate layer (bright) towards the outer surface. The same N_2 gas bubbles caused the porosity, noticed on the surface of sialon 1 (Fig. 8(a)). In some regions, cristobalite (dark grains) can be seen at the surface. The cracks might have been formed during cooling because of the difference in thermal expansion coefficient between oxide layer and sialon material.

The micrographs of sialon 2 (Fig. 8(b) and Fig. 9(b)), show the formation of elongated mullite crystals (bright) preferentially at the surface of the oxide layer. Beneath these mullite crystals, an amorphous aluminosilicate layer can be found. The formation of mullite might be explained by the higher Al content in the outer layer of the oxide scale. The mullite layer at the surface might act as a diffusion barrier for O_2, increasing the oxidation resistance. Cristobalite was not found in the oxide layer of sialon 2.

The micrographs of sialon 3 (Fig. 8(c) and Fig. 9(c)) show the formation of mullite crystals through the whole oxide layer. These mullite crystals are embedded in aluminosilicate glass, that is clearly concentrated in the protrusions on the surface. No porosity could be found in the oxide layer.

The morphology of the oxidized surface of sialon 4 (Fig. 8(d)) and sialon 5 (Fig. 8(e)) is the same as for sialon 3. The inhibition of the outward diffusion of N_2 by the mullite crystals is obvious from the porosity formed in the oxide layer (Fig. 9(d) and Fig. 9(e)). The oxide layer of sialon 5 is

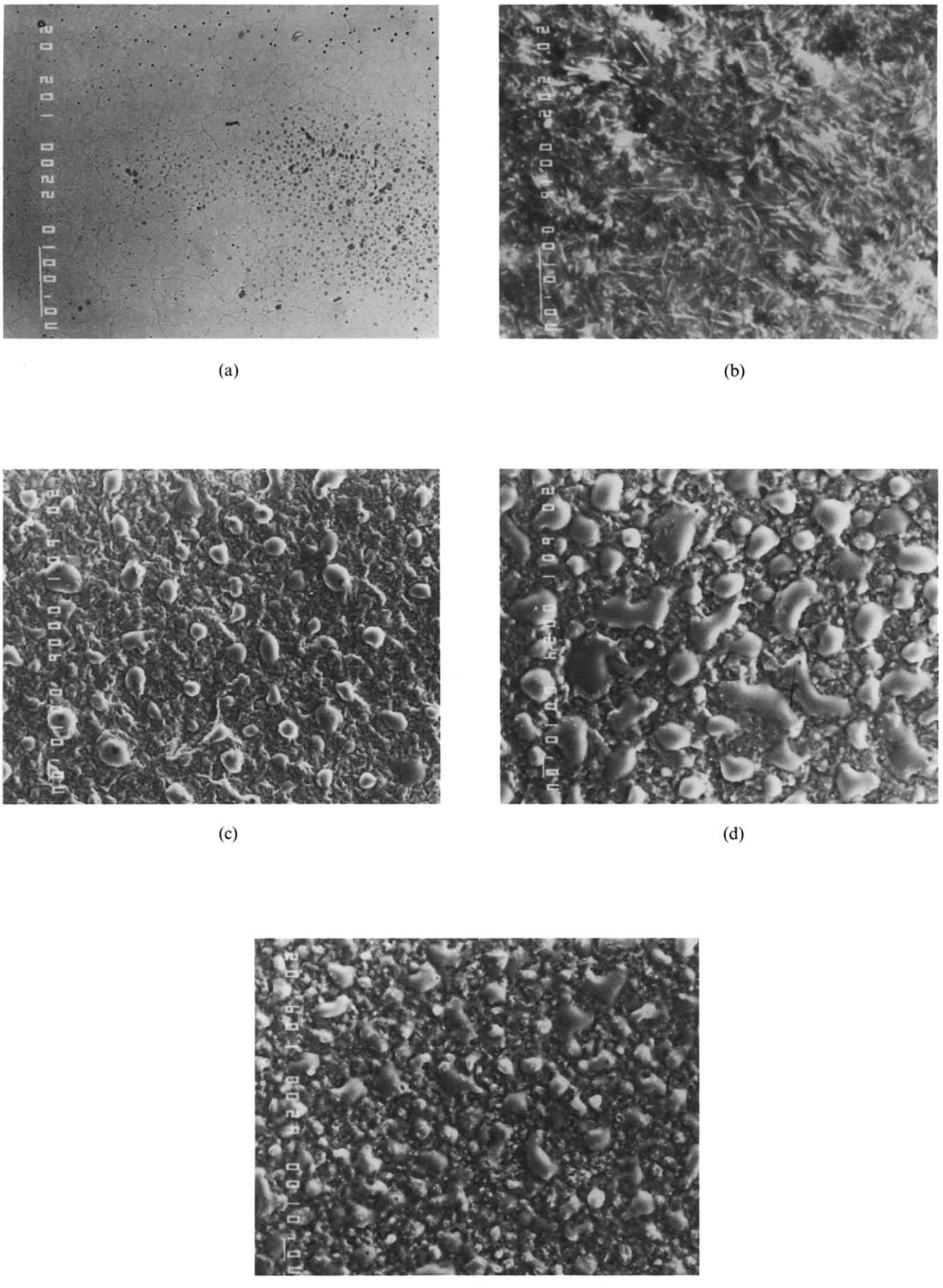

Fig. 8. Scanning electron micrographs of the surfaces formed in air after 160 h at 1300°C. (a) Sialon 1, (b) sialon 2, (c) sialon 3, (d) sialon 4 and (e) sialon 5.

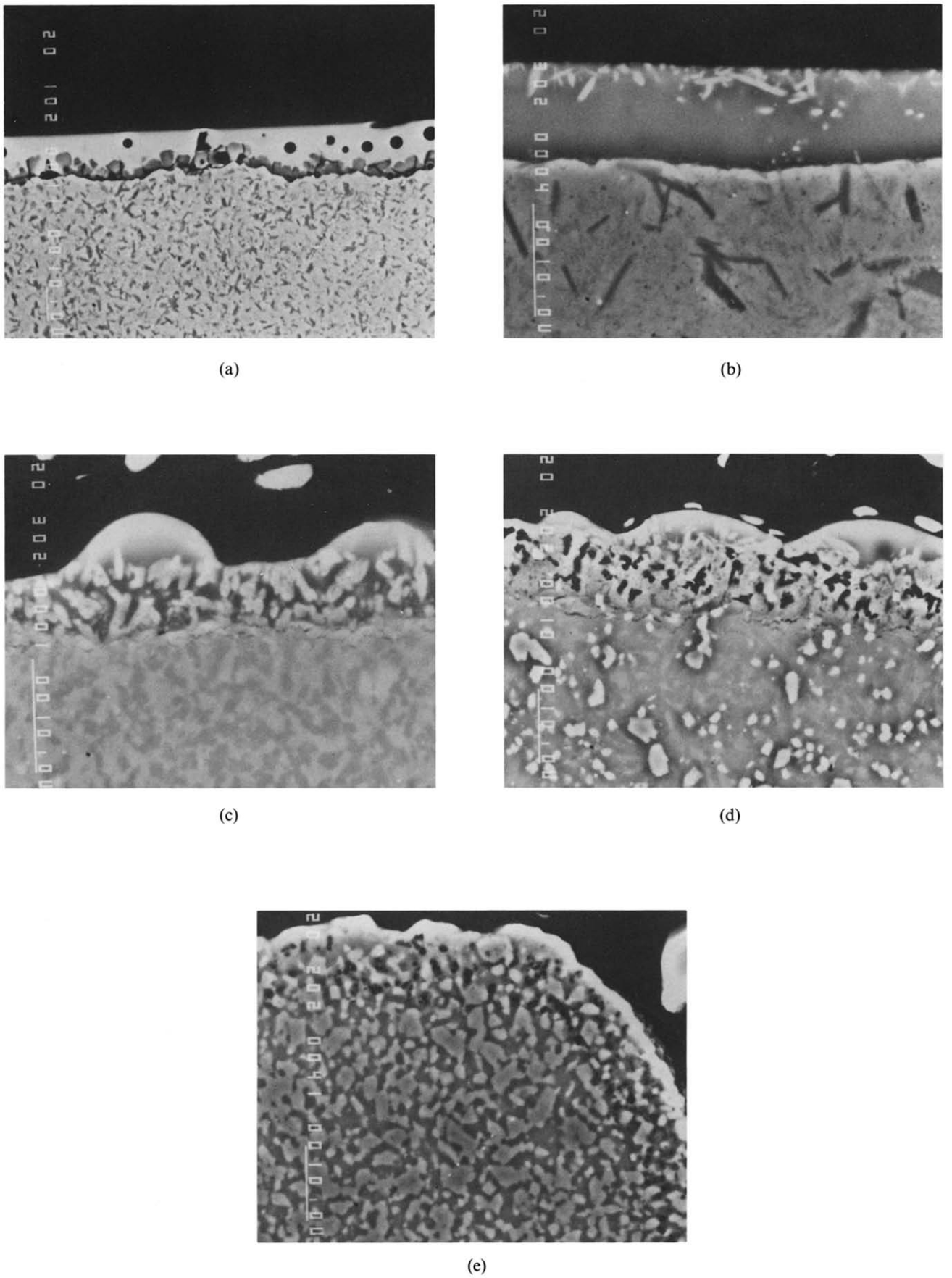

Fig. 9. Scanning electron micrographs of the cross-sections perpendicular to the oxide layer formed in air after 160 h at 1300°C (a) Sialon 1, (b) sialon 2, (c) sialon 3, (d) sialon 4 and (e) sialon 5.

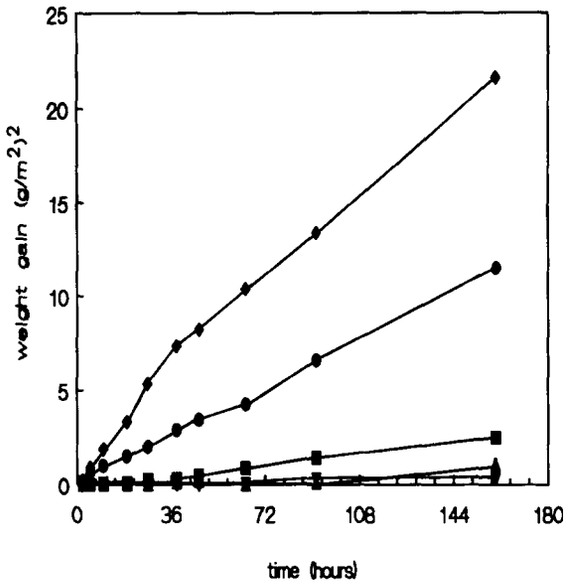

Fig. 10. Parabolic weight gain versus time plots, for the oxidation in air at 1300°C. ♦, Sialon 1; ●, sialon 2; ▼, sialon 3; ▲, sialon 4 and ■, sialon 5.

formed by alumina grains and pores in a mullite matrix. Glass could only be found in the protrusions on the surface.

The parabolic weight gain versus time plot (Fig. 10) shows a clearly parabolic and hence diffusion-controlled oxidation behaviour of the five different sialon materials at 1300°C. A break in the parabolic plot for sialon 1 is observed after 45 h of oxidation. For longer times, oxidation is still parabolic but with a decreased rate constant. A possible explanation might be that in the initial stage, N_2 gas bubbles moving towards the surface disrupt the formation of a stable oxide layer. At longer oxidation times, enough amorphous aluminosilicate is present to form a stable layer for the inward and outward diffusion of O_2 and N_2 respectively.

Despite the presence of cristobalite at the oxidation front, sialon 1 has a lower oxidation resistance than sialon 2. This can be explained by the higher amount of impurity ions in the glass phase of sialon 1, reducing the viscosity and enhancing O_2 transport, and by the O_2 diffusion limiting mullite crystals formed at the surface of sialon 2.

The lower oxidation rate of sialons 3, 4 and 5 can be attributed to the presence of mullite in the oxide layer. The reason for the higher oxidation rate of sialon 5, compared to sialon 3 and 4 is not clear. It is possible that in the absence of a minimum amount of glass, O_2 penetration through the open porosity, formed by volume changes during the crystallization of mullite and the increasing N_2 pressure, can not be prevented and internal oxidation is taking place.

3.4.3 Oxidation at 1450°C

Figures 11 and 12 show the surface and cross-section of the oxide layers formed in air after 100 h at 1450°C.

The SEM micrograph of sialon 1 (Fig. 11(a)) shows the development of large transparent gas-filled glass bubbles on the surface. The cross-section (Fig. 12(a)) shows the presence of SiO_2 crystals at the oxidation front. The glass bubbles were clearly visible after 20 h of oxidation.

White, non-transparent bubbles can be seen on the surface of sialon 2 (Fig. 11(b)). The cross sections (Fig. 12(b) and (c)) show that some of these bubbles are completely filled by mullite crystals, homogeneously embedded in an aluminosilicate glass matrix. In the contact zone between glass bubbles and non-oxidized sample, large voids can be seen. These voids might be caused by accumulation of N_2 gas. The phenomenon of glass-filled bubbles might be explained by a poor wetting behaviour of liquid aluminosilicate glass on sialon materials. At 1450°C, the glass is completely liquid as can be deduced from the metastable phase diagram of Al_2O_3–SiO_2.[33] The molar composition at the oxidation front can be calculated from the starting powder composition. The composition is 89 mol % SiO_2 and 11 mol % Al_2O_3. This is close to the eutectic point in the phase diagram. A similar glass-bubble formation was observed during oxidation of a sialon material after 8 hours at 1550°C.[35]

The oxidized surface of sialon 3 is very rough with large cracks (Fig. 11(c)). The cross-section (Fig. 12(d)) shows the formation of large porosities concentrated at the oxidation front. In the oxide layer, mullite crystals can be easily distinguished from the glass phase.

Sialon 4 shows more perpendicular to the surface oriented mullite crystals, embedded in aluminosilicate glass (Fig. 11(d)). Porosity is distributed throughout the oxide layer (Fig. 12(e)).

Aluminosilicate glass could not be found in the oxide layer of sialon 5 (Fig. 11(e) and Fig. 12(f)). The oxide layer consists of mullite with isolated Al_2O_3 crystals from the bulk material. Small pores seemed to be lined up to form channels between the surface and the oxidation front.

The parabolic weight gain versus time plots, for the oxidation experiment in air at 1450°C, are given in Fig. 13.

At oxidation times below 20 h, the oxidation behaviour of the sialon materials is parabolic. The oxidation resistance of sialon 1 is higher than that of sialon 2 because of the presence of SiO_2 crystals at the oxidation front. Cristobalite, known to be an effective barrier to oxygen permeation, was also associated with the passivation during oxidation of Si_3N_4–Y_2O_3 ceramics.[36,37] The oxidation sequence at short oxidation times of sialons 3, 4

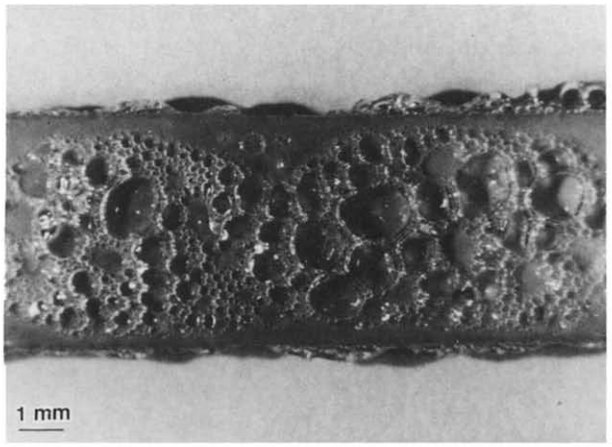

(a)

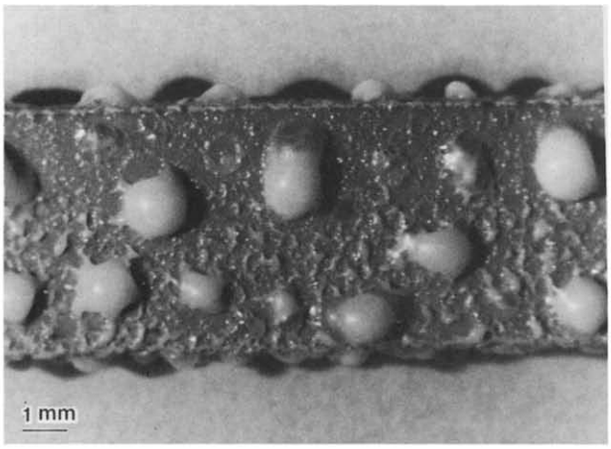

(b)

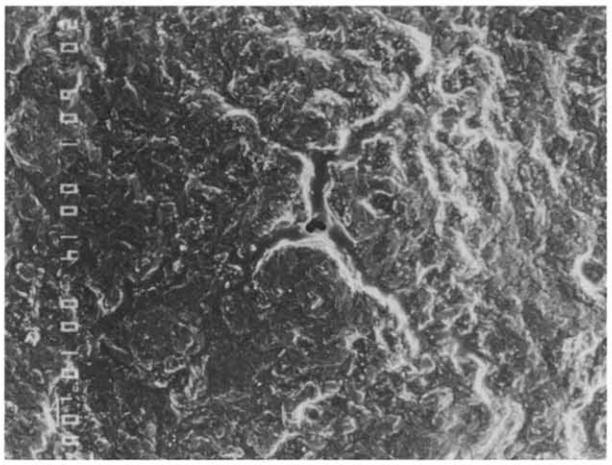

(c)

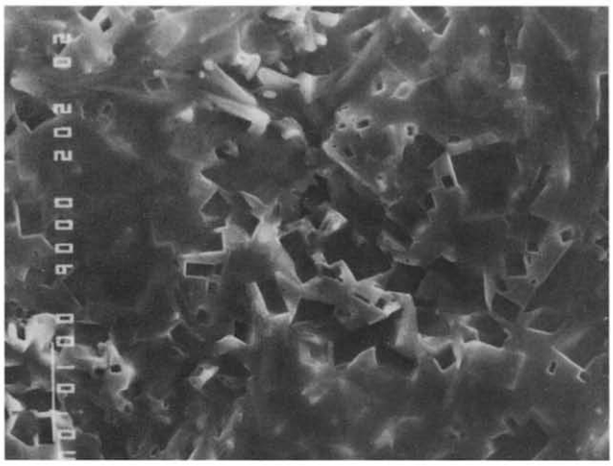

(d)

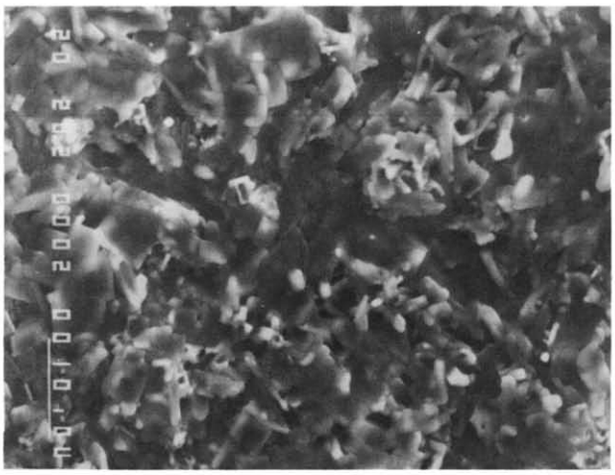

(e)

Fig. 11. Scanning electron micrographs of the surfaces formed in air after 100 h at 1450°C. (a) Sialon 1, (b) sialon 2, (c) sialon 3, (d) sialon 4 and (e) sialon 5.

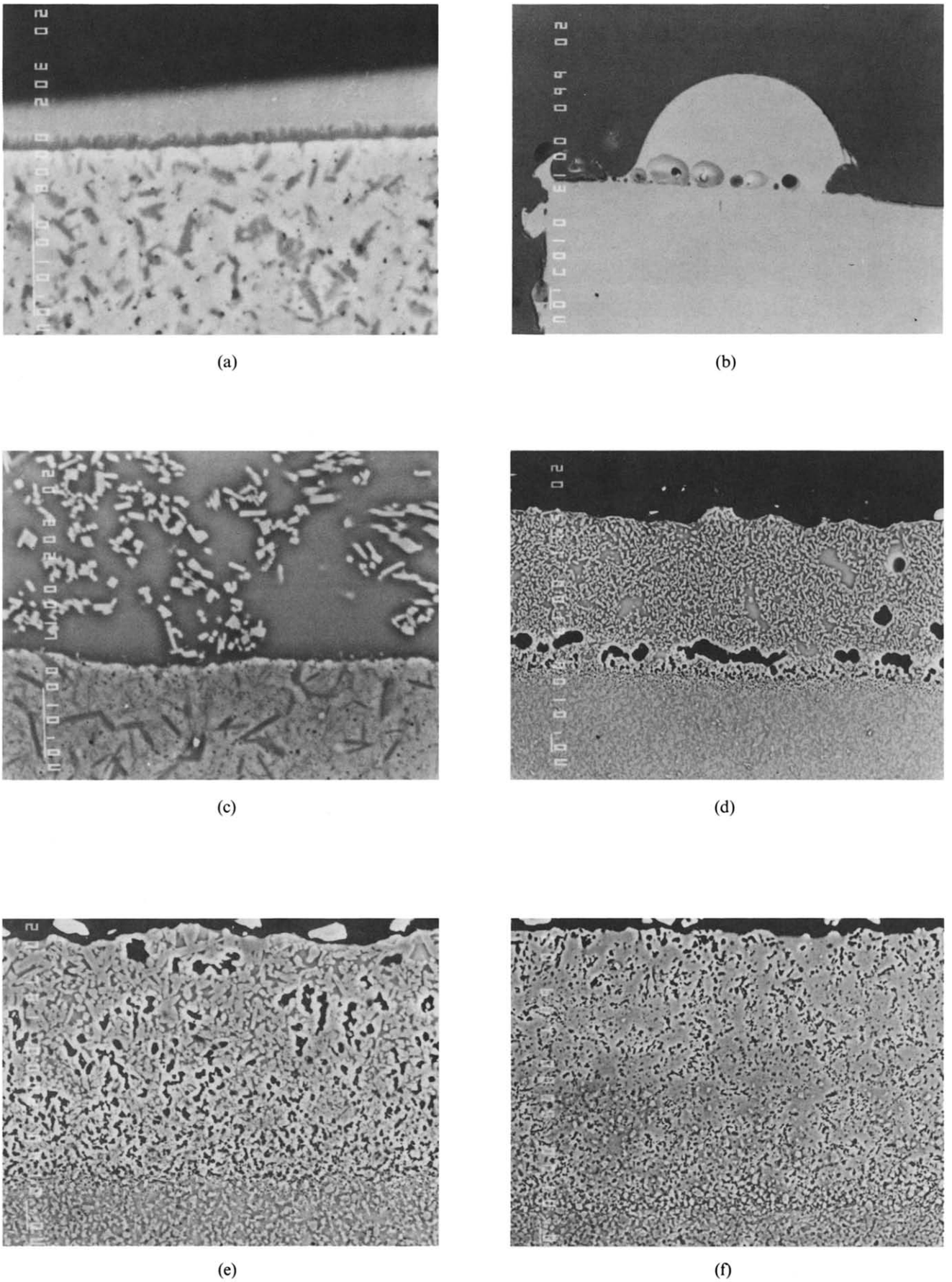

(a) (b)

(c) (d)

(e) (f)

Fig. 12. Scanning electron micrographs of the cross-sections perpendicular to the oxide layer formed in air after 100 h at 1450°C. (a) Sialon 1, (b) sialon 2, (c) sialon 2, (d) sialon 3, (e) sialon 4 and (f) sialon 5.

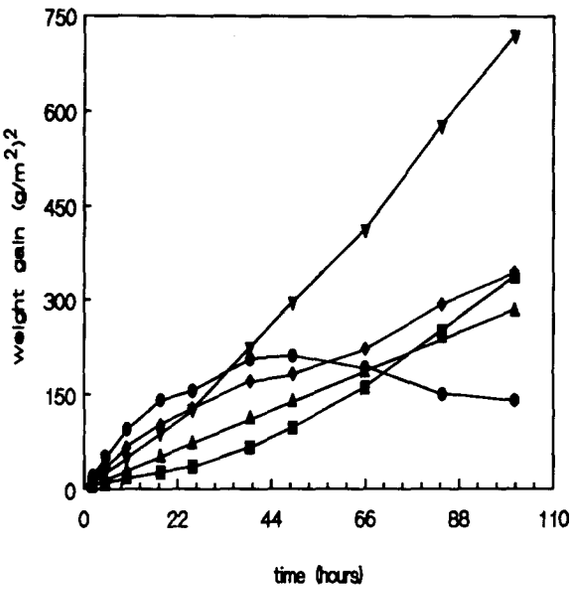

Fig. 13. Parabolic weight gain versus time plots, for the oxidation in air at 1450°C. ◆, sialon 1; ●, sialon 2; ▼, sialon 3; ▲, sialon 4 and ■, sialon 5.

and 5 is controlled by the increasing amount of mullite and the decreasing amount of aluminosilicate glass in the oxide layer.

At longer oxidation times, the oxidation curves become more complex. The parabolic oxidation rate constant of sialon 4 is constant up to 100 h oxidation time. The oxidation rate of sialons 3 and 5 increases. The oxidation rate of sialons 1 and 2 decreases.

The change in oxidation rate of sialons 1 and 2 can be explained by the O_2 diffusion limiting and/or oxidation surface decreasing effect of the gas- or glass-filled bubbles at the surface of the oxidation layer. A comparable change in oxidation rate was observed during oxidation of Si_3N_4 after 16 h in O_2 at 1450°C.[38] The reason for the decreasing curve of sialon 2 at longer oxidation times is not clear.

The cross-sectioned oxide layer of sialon 3 shows large porosities concentrated at the oxidation front. Because of the rather high amount of liquid aluminosilicate, N_2 gas is easily concentrated to form large bubbles close to the oxidation front. As oxidation proceeds, the N_2 pressure will exceed a certain level, causing lifting of the oxide layer and the formation of large pores (Fig. 12(d)). A connection between surface and gas bubbles is formed, allowing the N_2 gas to escape. After gas release, the pores are probably filled with liquid glass. This explains the existence of larger mullite-free glass regions and the absence of pores in the outer zone of the oxide layer. These mullite-free regions might also improve O_2 diffusion, explaining the oxidation rate increase at longer oxidation time.

Because of the lower amount of glass in the oxide layer of sialon 4, the formation of large N_2 bubbles is inhibited and the oxidation mechanism as postulated for sialon 3 is less pronounced. O_2 diffusion through the glass phase probably remains the oxidation-controlling mechanism, even at long oxidation times.

No glass phase could be found in the oxide layer of sialon 5. The increase in oxidation rate constant can only be explained by the formation of open porosity through the mullite matrix layer.

4 Conclusions

TEM investigation showed that O'- and X-sialon grains can be easily distinguished from the hexagonal β-sialon particles by their high stacking fault density and twin pattern respectively. Within the resolution limit of the TEM, no evidence could be found for the presence of an amorphous grain-boundary phase, although the presence of a very small grain-boundary phase, a few atomic layers thick, is not excluded.

Chemical analysis of the different phases was possible by EPMA. The maximum solubility of Al_2O_3 in Si_3N_4 at 1650°C is lower than might be expected from reported phase diagrams. The chemical composition of X-sialon is $Si_{12}Al_{18}O_{39}N_8$, one of the nine different compositions found in the literature. A revised phase diagram at 1650°C is proposed, taking into account the limited extension of the β'-phase at lower temperatures.

A high hardness, but rather modest fracture toughness was measured for the β–O'-sialon materials. It is clear that the presence of large amounts of X-sialon is detrimental to the mechanical properties of sialon materials. The presence of isolated α-Al_2O_3 grains counteracts the negative effect of X-sialon.

The metastable phase diagram[33] of Al_2O_3–SiO_2 in the absence of mullite can be used to predict the oxidation products and relative amounts formed in the oxide layers of Si_3N_4–Al_2O_3 sialon materials in air at 1300°C and 1450°C. The oxide layers of sialons with an overall molar composition at the oxidation front below the eutectic composition will consist of cristobalite and an amorphous aluminosilicate phase. At compositions above the eutectic, mullite and aluminosilicate is formed.

The oxidation resistance of sialon materials is controlled by the composition and amount of the amorphous aluminosilicate phase, the presence of cristobalite and mainly by the O_2 diffusion-limiting effect of mullite crystals. The aluminosilicate phase formed during oxidation contains a small amount of impurity ions (Ca, Mg and Na), that

are thought to be diffusing outwards from the grain boundaries in the bulk material into the oxide layer during oxidation.

At 1300°C, oxidation is controlled by the diffusion of O_2 through the aluminosilicate phase. The oxidation resistance increases with increasing Al_2O_3 content in the starting powder, although a minimum amount of glass is necessary to prevent a decrease in oxidation resistance at higher Al_2O_3 content.

At oxidation times below 20 h at 1450°C, sialons show a parabolic oxidation behaviour. The lowest oxidation resistance was found for the sialon with an overall composition at the oxidation front that was close to the eutectic composition in the Al_2O_3–SiO_2 phase diagram. The Si_3N_4-richer sialon showed an increased resistance because of the presence of SiO_2 crystals in the oxide layer. The oxidation resistance of the Al_2O_3-richer sialons increased with increasing Al_2O_3 content of the starting powder. At longer oxidation times at 1450°C, oxidation behaviour becomes very complex.

Acknowledgements

The authors wish to thank Dr T. Laoui for his assistance with the TEM work. J. V. thanks the Belgian I.W.O.N.L. fund for a research fellowship. This work was also supported by the Brite-Euram programme of the Commission of the European Communities under project BREU-0096-C.

References

1. Ziegler, G., Heinrich, J. & Wotting, W., Review: relationships between processing, microstructure and properties of dense and reaction-bonded silicon nitride. *J. Mater. Sci.*, **22** (1987) 3041–86.
2. Komanduri, R. & Samanta, S. K., Ceramics. In *Metals Handbook, Machining*, Vol. 16. ASM International, OH, 1989, pp. 98–104.
3. Jack, K. H., Review: sialon and related nitrogen ceramics. *J. Mater. Sci.*, **11** (1976) 1135–58.
4. Oyama, Y. & Kamigaito, O., Hot-pressing of Si_3N_4–Al_2O_3. *Yogyo-Kyokai-Shi*, **80** (1972) 327–36.
5. Ekström, T., Käll, P. O., Nygren, M. & Olsson, P. O., Dense single-phase β-sialon ceramics by glass-encapsulated hot isostatic pressing. *J. Mater. Sci.*, **24** (1989) 1853–61.
6. Lewis, M. H., Powell, B. D., Drew, P., Lumby, R. J., North, B. & Taylor, A. J., The formation of single-phase Si–Al–O–N ceramics. *J. Mater. Sci.*, **12** (1977) 61–74.
7. Gauckler, L. J., Prietzel, S., Bodemer, G. & Petzow, G., Some properties of β-$Si_{6-x}Al_xO_xN_{8-x}$. In *Nitrogen Ceramics*, ed. F. L. Riley. Noordhoff, Leyden, The Netherlands, 1977, pp. 529–37.
8. Naik, I. K., Gauckler, L. J. & Tien, T. Y., The solid–liquid equilibria in the system Si_3N_4–AlN–SiO_2–Al_2O_3. *J. Am. Ceram. Soc.*, **61** (1978) 332–5.
9. Washburn, M. E., Silicon oxynitride refractories. *Am. Ceram. Soc. Bull.*, **46** (1967) 667–71.
10. Zangvil, A., The structure of the *X* phase in the Si–Al–O–N alloys. *J. Mater. Sci. Lett.*, **13** (1978) 1370–4.
11. Thompson, D. P. & Korgul, P., Sialon *X*-phase. In *Progress in Nitrogen Ceramics*, ed. F. L. Riley. Martinus Nijhoff, The Hague, The Netherlands, 1983, pp. 375–80.
12. Mitomo, M., Hasegawa, Y., Bando, Y., Watanabe, A. & Suzuki, H., The strength of hot-pressed β-sialon. *Yogyo-Kyokai-Shi*, **88** (1980) 298–304.
13. Gauckler, L. J., Lucas, H. L. & Petzow, G., Contribution to the phase diagram Si_3N_4–AlN–Al_2O_3–SiO_2. *J. Am. Ceram. Soc.*, **58** (1975) 346–7.
14. Wills, R. R., Stewart, R. W. & Wimmer, J. M., Effect of composition and *X*-phase on the intrinsic properties of reaction-sintered sialon. *Am. Ceram. Soc. Bull.*, **56** (1977) 194–203.
15. Zangvil, A., Gauckler, L. J. & Rühle, M., Indexed X-ray diffraction data for the sialon *X*-phase. *J. Mater. Sci. Lett.*, **15** (1980) 788–90.
16. Bergman, B., Ekström, T. & Micski, A., The Si–Al–O–N system at temperatures of 1700–1775°C. *J. Eur. Ceram. Soc.*, **8** (1991) 141–51.
17. Lewis, M. H. & Barnard, P., Oxidation mechanisms in Si–Al–O–N ceramics. *J. Mater. Sci.*, **15** (1980) 443–8.
18. Lewis, M. H., Bhatti, A. R., Lumby, R. J. & North, B., The microstructure of sintered Si–Al–O–N ceramics. *J. Mater. Sci.*, **15** (1980) 103–13.
19. Singhal, S. C., Thermodynamics and kinetics of oxidation of hot-pressed silicon nitride. *J. Mater. Sci.*, **11** (1976) 500–9.
20. Schlichting, J. & Gauckler, L. J., Oxidation of some β-Si_3N_4 materials. *Powd. Met. Int.*, **9** (1977) 36–9.
21. Takase, A., Investigation of the oxidation of sialons with infrared reflection spectroscopy. *J. Mater. Sci.*, **21** (1986) 329–34.
22. Hasegawa, Y. T., Hirota, K., Yamane, T., Mitomo, M. & Suzuki, H., Oxidation behaviour of hot-pressed sialon. *Yogyo-Kyokai-Shi*, **89** (1981) 148–55.
23. JCPDS, International Centre for Diffraction Data, Powder Diffraction Files, 1601 Park Lane, Swarthmore, USA.
24. Anstis, G. R., Chantikul, P., Lawn, B. R. & Marshall, D. B., A critical evaluation of indentation techniques for measuring fracture toughness: I. Direct crack measurements. *J. Am. Ceram. Soc.*, **64** (1981) 533–8.
25. Jack, K. H., The relationship of phase diagrams to research and development of sialons. In *Phase Diagrams, Materials Science and Technology*, Vol. 5, ed. A. M. Alper. Academic Press, London, 1978, pp. 241–83.
26. Lewis, M. H., Reed, C. J. & Butler, N. D., Pressureless-sintered ceramics based on the compound Si_2N_2O. *Mater. Sci. Eng.*, **71** (1985) 87–94.
27. Trigg, M. B. & Jack, K. H., Solubility of aluminium in silicon oxynitride. *J. Mater. Sci. Lett.*, **6** (1987) 407–8.
28. Anya, C. C. & Hendry, A., Stoichiometry and crystal structure of *X*-phase sialon. *J Eur. Ceram. Soc.*, **10** (1992) 65–74.
29. Hillert, M. & Jonsson, S., Thermodynamic calculation of the Si–Al–O–N system. *Z. Metallkd.*, **83** (1992) 720–8.
30. Jack, K. H., Sialon tool materials. *Metals Technology*, **9** (1982) 297–301.
31. Johnson, P. M. & Hendry, A., The microstructure of hot-pressed sialon polytypes. *J. Mater. Sci.*, **14** (1979) 2439–45.
32. Gauckler, L., Lukas, H., Henig, E. & Petzow, G., Representation of phase equilibria in the systems with a double exchange reaction. *Calphad*, **2** (1978) 349–56.
33. Risbud, S. H. & Pask, J. A., SiO_2–Al_2O_3 metastable phase equilibrium diagram without mullite. *J. Mater. Sci.*, **13** (1978) 2449–54.
34. Aksay, I. A., Dabbs, D. M. & Sarikaya, M., Mullite for structural, electronic and optical applications. *J. Am. Ceram. Soc.*, **74** (1991) 2343–58.

35. Desmaison, J. G. & Riley, J. F., The oxidation in air of sialon materials formed without densification aids. *J. Mater. Sci. Lett.*, **16** (1981) 2625–8.
36. Andrews, P. & Riley, F. L., The microstructure and composition of oxide films formed during high temperature oxidation of a sintered silicon nitride. *J. Eur. Ceram. Soc.*, **5** (1989) 245–56.
37. Castro, F., Echeberria, J. & Fuentes, M., High-temperature oxidation resistance and microstructures of the oxide films in silicon nitride ceramics. *J. Mater. Sci. Lett.*, **11** (1992) 101–5.
38. Tripp, W. C. & Graham, H. C., Oxidation of Si_3N_4 in the range 1300°C to 1500°C. *J. Am. Ceram. Soc.*, **59** (1976) 399–403.